Using Simulations to Probe the Narrow-Line Region of AGN in Galaxy Mergers

Laura Blecha, Abraham Loeb, & Ramesh Narayan

14 September 2011

ABSTRACT

1 INTRODUCTION

Although the hierarchical-growth paradigm suggests that super-massive black hole (SMBH) pairs should be common through the history of the Universe, until recently, evidence for their existence has been scarce. Because of the vast dynamic range involved in bringing SMBHs from galactic scales to within a few gravitational radii of each other, searches for SMBH pairs must target a specific phase of this evolution. On the largest scales, when the BHs simply follow the motion of their host galaxies, some constraints are obtained from quasar clustering surveys. About 0.1% of quasars are known to be in pairs on scales of ~ 100 kpc [cite]; however, on these large scales it is unclear whether the nuclear activity is actually associated with galaxy interactions. When the galaxies are in the later stages of merging and the BH separation is $\sim 1 - 10$ kpc, dynamical friction drives the evolution of the BH pair toward the center of the merger remnant. This "kiloparsec-scale" phase has seen by far the most recent progress in identification of candidate SMBH pairs. A handful of resolved AGN pairs on these scales have been found serendipitously (Komossa et al. 2003; Bianchi et al. 2008; Green et al. 2010), but spectroscopic surveys of AGN have recently demonstrated that about 1% of all AGN have double-peaked narrow [O III] lines, a possible signature of SMBH orbital motion on kpc scales (Comerford et al. 2009a; Smith et al. 2009; Liu et al. 2009). These findings essentially increased the number of candidate SMBH pairs to more than 200. While only a fraction of these double-NL (dNL) AGN are actually expected to contain SMBH pairs, follow-up imaging has already revealed strong evidence that some of these are in fact dual SMBHs (Shen et al. 2011) [others...]. Therefore, this spectroscopic method appears to be a promising avenue for identifying and studying SMBH pairs.

On smaller scales (~ 10 pc to $\ll 1$ pc), BH pairs evolve to form a true bound binary BH. These present a formidable challenge for observers, partly because they are difficult if not impossible to resolve. Additionally, there is still much uncertainty regarding the timescale required for the binary to evolve from scales of a few pc down to miliparsec scales where GW emission dominates the orbital decay. It has been shown that in highly symmetric, spheroidal galaxies with little to no gas, BH binaries may "stall" at ~ 1 pc for more than a Hubble time (e.g., Begelman et al. 1980; Milosavljević & Merritt 2001; Yu 2002) – i.e., they never reach the final, GW-driven phase of merging. If the galaxy is gas-rich or substantially triaxial, however, the BHs may merge on a much shorter timescale ($\sim 10^6 - 10^7$ yr from the hard binary stage; e.g., Gerhard & Binney 1985; Yu 2002; Berczik et al. 2006; Escala et al. 2004; Gould & Miralda-Escude 1997). Only one confirmed example of a bound

SMBH binary is known, with a 7 pc separation. (Rodriguez et al. 2006). Two sub-parsec (spectroscopic) binary candidates have been proposed recently but have not been confirmed (Dotti et al. 2008; Bogdanović et al. 2009; Boroson & Lauer 2009).

Theoretical studies of SMBH mergers face their own challenges, largely owing to the vast range in physical scales involved. Significant progress has been made on the smallest scales; simulations of BH mergers using full general relativity are now possible and can generate precise waveforms of GW emission as well as the remnant BH properties [cite]. On galactic scales, interactions and mergers have been studied extensively with hydrodynamic simulations [cite]. In relative terms, BH evolution on intermediate scales is quite poorly understood, although as illustrated above this regime is currently the most active focus of observational studies. In particular, little has been done to understand the nature of double-peaked narrow-line (NL) AGN. Galaxy merger simulations have not considered the NL region (NLR), and detailed photoionization models have not been applied to the rapidly-varying environment of a late-stage merger. Here, we make a first attempt to model the NLR during galaxy mergers using hydrodynamic simulations, with special attention to the kiloparsec-scale phase that may produce double-peaked NL AGN.

This paper is organized as follows. In § 2.1 & 2.2, we describe our simulations and galaxy merger models. Our semianalytic model for the narrow-line gas, which is implemented in post-processing, is detailed in § 2.3 - § 2.4. Our results are presented in § 3. In § 3.1, we describe the evolution of the NLR throughout a major merger, and discuss dependence on merger parameters. We describe the morphological properties of the NLRs in § 3.2, and in § 3.3 we explore the observable signatures of kiloparsec-scale double-NL AGN. The lifetimes of double-NL AGN are discussed in § 3.4. Finally, we summarize and discuss our results in § 4. Throughout the paper, we assume a flat ΛCDM cosmology with $H_0 = 71$ km s^{-1} Mpc^{-1}, $\Omega_m = 0.27$, and $\Omega_\Lambda = 0.73$.

2 METHODS

2.1 Simulations

We use GADGET-3 for our numerical studies of SMBH mergers. GADGET is a smoothed-particle hydrodynamics (SPH) code that conserves both energy and entropy (Springel 2005). The version we use includes radiative cooling as well as a subresolution model for a multiphase interstellar medium (ISM, Springel & Hernquist 2003) that accounts for star formation and supernova feedback. In

addition, the code models BHs as gravitational "sink" particles that contain a BH seed and a gas reservoir. The reservoir is replenished by stochastic accretion of neighboring gas particles, but the actual accretion rate onto the BH is calculated smoothly using the Bondi-Hoyle formula (Bondi & Hoyle 1944) with locally-averaged values for the density and sound speed. Angular momentum is conserved during accretion of gas particles, but because this a stochastic process we also introduce an accretion drag force calculated from the Bondi accretion rate. These prescriptions are described in more detail in Springel et al. (2005).

2.2 Galaxy Merger Models

The progenitor galaxies for our merger simulations consist of a dark matter halo, a disk of gas and stars, and a central BH sink particle as described above. We also include a stellar bulge component to some models. We use fairly high mass and spatial resolution in order to resolve as best as possible the NLR around each BH. The gravitational softening length adopted is 37 pc, and the mass resolution is [**list for each particle type**]. Each galaxy is given a single BH with a seed mass of 2×10^5 M$_\odot$; the small value chosen reflects the fact that our galaxies are initially bulgeless. The galaxies are set on a parabolic orbit with an initial separation of 100 h^{-1} kpc. [**describe actual models used in more detail.**]

2.3 NLR Identification

Here we outline a basic procedure for determining the location, kinematics, and (Hβ) luminosity of the narrow-line region around one or more AGN in a gaseous galaxy merger simulation with GADGET-3 All of the calculations described here are done in post-processing, i.e. after the GADGET simulation has finished.

2.3.1 BH accretion & luminosity

We use the standard GADGET prescription for BH accretion; ie., the Bondi-Hoyle accretion rate, capped at the Eddington limit.

$$\dot{M} = \min(\dot{M}_{\rm Bondi}, \dot{M}_{\rm Edd}), \tag{1}$$

$$\dot{M}_{\rm Bondi} = \frac{4\pi (G M_{\rm BH})^2 \rho_{\rm g,\infty}}{(v_{\rm rel}^2 + c_{\rm s,\infty}^2)^{3/2}} \tag{2}$$

$$\dot{M}_{\rm Edd} = \frac{4\pi G M_{\rm BH}}{0.1 \kappa_{\rm es} c} \tag{3}$$

where $v_{\rm rel}$, $c_{\rm s,\infty}$, and $\rho_{\rm g,\infty}$ are all computed as averages over the gas particles neighboring the BH. The Eddington value assumes a radiative efficiency of 0.1. Using this accretion rate, we can calculate a bolometric luminosity

$$L_{\rm bol} = \eta \dot{M} c^2, \tag{4}$$

where the radiative efficiency η is assumed to be 0.1 unless $\dot{M} \ll \dot{M}_{\rm Edd}$, in which case the BH is assumed to be radiatively inefficient, with the following scaling for η (Narayan & McClintock 2008):

$$\eta = 0.1 \left(\frac{\dot{M}}{0.01 \dot{M}_{\rm Edd}} \right), \quad \dot{M} < 0.01 \dot{M}_{\rm Edd}. \tag{5}$$

2.3.2 Ionizing photon production rate

To calculate properties of the NL region, we need to know the number of ionizing photons produced by the accreting BHs. We begin

by applying a reverse bolometric correction to $L_{\rm bol}$ to obtain the B-band luminosity, and then we assume a broken power-law form for the optical - UV spectrum. Following the method of Marconi et al (2004), the bolometric correction is:

$$\log \left(\frac{L_{\rm bol}}{\nu_{\rm B} L_{\nu_{\rm B}}} \right) = 0.8 - 0.067 \mathcal{L} + 0.017 \mathcal{L}^2 - 0.0023 \mathcal{L}^3, \tag{6}$$

where $\mathcal{L} = \log L_{\rm bol} - 12$ and $L_{\rm bol}$ is in units of $L_\odot$. For the broken power-law, we use the following spectral indices from the AGN SED fits of Marconi et al. (2004):

$$\alpha_{\rm opt} = -0.44, \quad 1\,\mu{\rm m} > \lambda > 1300\text{Å} \tag{7}$$

$$\alpha_{\rm UV} = -1.76, \quad 1200\text{Å} > \lambda > 500\text{Å}. \tag{8}$$

Then we can get the normalization factor $A_{\rm opt}$ from the bolometric correction by taking $\nu_{\rm B} L_{\nu_{\rm B}} = A_{\rm opt} \nu_{\rm B}^{\alpha_{\rm opt}+1}$. To get the normalization for the UV range we can take $\nu L_\nu(1300\text{Å}) = \nu L_\nu(1200\text{Å})$, which gives

$$\frac{A_{\rm UV}}{A_{\rm opt}} = 2.02 \times 10^{20}. \tag{9}$$

The normalization $A_{\rm UV}$ allows us to calculate the number of ionizing photons emitted per unit time by the source:

$$Q = \int_{\nu_0}^{\infty} \frac{L_\nu}{h\nu} d\nu. \tag{10}$$

2.3.3 Selection criterion for cold-phase gas

In order to determine which gas in the galactic center will be ionized by this radiation and produce narrow-line emission, we must impose several criteria on the SPH particles. The multiphase model for the ISM in GADGET assumes that the gas is comprised of a "cold" phase and a "hot" phase, which can exchange mass via star formation, cooling, and evaporation from supernovae. First, we select only those gas particles that have a nonzero fraction of mass $f_{\rm cold}$ in the "cold" phase. We assume that the cold-phase gas has fragmented into discrete clouds on sub-resolution scales. The NL clouds are heated by photoionization and should be warmer than the cold clouds in the multiphase ISM ($\sim 10^4$ K versus $\sim 10^3$ K) and thus less dense (assuming pressure equilibrium between phases). Therefore, we use the parameters of the multiphase model only for selection of SPH particles that contain cold gas, and we instead calculate a "cloud density" for each of these particles: $\rho_{\rm cl} = \rho_{\rm sph} T_{\rm sph} / 10^4$ K. (Here, the subscript "sph" denotes that these quantities are averaged between the hot and cold phases, and the subscript "cl" denotes the quantities for our NL cloud model.)

2.3.4 Selection criterion for gas particle covering fraction

We also impose a criterion on the SPH particles such that the solid angle subtended by NL clouds does not exceed 4π. We cannot determine exactly which clouds will have unobscured sight lines to the AGN, as their size is below our resolution limit and our simulations do not include radiative transfer. However, we account for the problem of particle self-blocking in an average sense, as follows. An SPH particle that subtends a solid angle $\Omega_{\rm sph}$ has a covering fraction

$$f_{\Omega_{\rm sph}} = \frac{\Omega_{\rm sph}}{4\pi} = \frac{r_{\rm sph}^2}{4\,r_{\rm BH}^2}, \tag{11}$$

$$r_{\rm sph} = \left(\frac{m_{\rm sph}}{\frac{4\pi}{3} \langle \rho \rangle} \right)^{1/3}, \tag{12}$$

where m_{sph} is the mass of the SPH particle, r_{sph} is the effective size of the particle and r_{BH} is the distance to the BH. The "area filling factor" (ϵ_{A}) and volume filling factor (ϵ_{V}) are the fractions of the SPH particle's area and volume covered by the cold clouds, respectively:

$$\epsilon_{\mathrm{A}} = \min\left(\epsilon_{\mathrm{V}}^{2/3}\, N_{\mathrm{cl}}^{1/3}\ ,\ f_{\mathrm{A}} \right), \tag{13}$$

$$\epsilon_{\mathrm{V}} = f_{\mathrm{cold}}\, \frac{\rho_{\mathrm{sph}}}{\rho_{\mathrm{cl}}}, \tag{14}$$

where f_{A} is described below, and $N_{\mathrm{cl}} = f_{\mathrm{cold}}\, m_{\mathrm{sph}}/m_{\mathrm{cl}}$ is the number of clouds within the particle. In this formulation, m_{cl} is a free parameter that serves mainly to set the surface area to volume ratio of the NL clouds. We assume that each cloud has a constant mass $m_{\mathrm{cl}} = 100 M_{\odot}$.

The above formula for ϵ_{A} is the *maximal* area filling factor when $f_{\mathrm{A}} = 1$, assuming a uniform distribution of clouds. In practice this almost always gives a value near or equal to unity for ϵ_{A}, regardless of the choice of m_{cl}. In reality, we may expect some clumpiness in the cloud distribution, so instead choose a lower value for f_{A}. From a practical standpoint, ensuring that ϵ_{A} is not too close to unity prevents an undesirable sensitivity of our results to the value of r_{sph}, especially for the innermost particles. In what follows we choose $f_{\mathrm{A}} = 0.2$.

The fractional solid angle subtended by the clouds in each particle is then

$$f_{\Omega} = \frac{\epsilon_{\mathrm{A}}\, \Omega_{\mathrm{sph}}}{4\pi}. \tag{15}$$

In order to avoid allowing multiple clouds to absorb the same photons, we truncate the NLR beyond the radius where the total covering fraction of clouds reaches unity. While this method is not exact, it does allow for the correct rate of ionization in an averaged sense.

2.3.5 Selection criteria for ionization parameter & density

For the remaining gas particles, we calculate the ionization parameter for the cold clouds in a given SPH particle when ionized by a single BH:

$$U = \frac{Q}{4\pi r_{\mathrm{BH}}^2 c\, n_{\mathrm{H,cl}}}, \tag{16}$$

where $n_{\mathrm{H,cl}} = \rho_{\mathrm{cl}}/\mu m_{\mathrm{H}}$ is the number density of the NL clouds and r_{BH} is the distance from the BH to the cloud. The ionization parameter quantifies the ratio of the ionizing photon density to the electron density at each cloud. In the case of a galaxy merger where two active BHs may be present, the ionization parameter becomes

$$U = \frac{1}{4\pi c\, n_{\mathrm{H,cl}}}\left(\frac{Q_1}{r_{\mathrm{BH1}}^2} + \frac{Q_2}{r_{\mathrm{BH2}}^2} \right), \tag{17}$$

where the subscripts "1" and "2" refer to the primary and secondary BHs. We select only particles with U in the range $10^{-4.5} - 10^{-1.5}$, based on results from photoionization models of NL regions (cf. Osterbrock & Ferland 2006).

Finally, we must ensure that the cloud densities themselves are reasonable. We therefore impose an additional cut on the SPH particles such that only those with $n_{\mathrm{H,cl}}$ in the range $10^2 - 10^6$ cm^{-3} are included (cf. Osterbrock & Ferland 2006). The maximum density is typically the more limiting criterion, and is chosen to be roughly equal to the critical density for [O III] emission. Above this density, collisional de-excitation begins to dominate over the forbidden-line

emission. While we do not consider forbidden lines in our model, we know they are present in real NLRs, and further that AGN typically have [O III]/H$\beta \gtrsim 3$. Thus, gas above the maximum density will not contribute to the NL AGN profile in a conventional manner, and we exclude these particles from our NL model.

2.3.6 Identification of gas particles with each BH

After the galaxies have undergone a close passage, and especially during their final coalescence, particles are easily exchanged between galaxies, and the initial identifications of which particles are in which galaxy are no longer relevant. Thus, we need criteria for assigning particles to each BH at any point in the simulation. When the galaxies are near coalescence, the identification of an SPH particle with one galaxy or the other is less physically meaningful, but it is still helpful for understanding the merger kinematics. Because we are concerned primarily with the relationship of gas particles to the central BHs, we assign particles to each galaxy based on their proximity to and degree of photoionization from each BH. Specifically, we switch gas particles from their initial galaxy identification if a) they are closer to the BH in the other galaxy and b) the quantity Q/r_{BH}^2 is four times larger for the BH in the other galaxy (i.e., $U_{1,2}/U_{2,1} > 4$).

2.4 Hβ Luminosity and Velocity Profiles

2.4.1 Hβ luminosity

Once we have selected SPH particles with cold-phase gas in the desired ranges of U and n_{H} that we believe should contain narrow-line emitting clouds, we may estimate the Hβ luminosity of each cloud, $L_{\mathrm{H}\beta}$. This can be written as

$$L_{\mathrm{H}\beta} = h\, \nu_{\mathrm{H}\beta}\, Q\, \frac{\alpha_{\mathrm{H}\beta}^{\mathrm{eff}}(T)}{\alpha_{\mathrm{B}}^{\mathrm{eff}}(T)}\, f_{\Omega}, \tag{18}$$

where Q is the rate of ionizing photon production as before, f_{Ω} is the cloud covering fraction discussed above, and $\alpha_{\mathrm{H}\beta}^{\mathrm{eff}}(T)/\alpha_{\mathrm{B}}^{\mathrm{eff}}(T) \approx 1/8.5$ is the number of Hβ photons produced per hydrogen recombination (for $T = 10^4$ K). Thus, when two ionizing sources (two BHs) are present, the total Hβ luminosity is

$$L_{\mathrm{H}\beta} = \frac{h\, \nu_{\mathrm{H}\beta}}{8.5}\, \frac{\epsilon_{\mathrm{A}}}{4\pi}\, \left(\Omega_{1,\mathrm{sph}}\, Q_1 + \Omega_{2,\mathrm{sph}}\, Q_2 \right). \tag{19}$$

2.4.2 Hβ velocity profiles

In order to understand the kinematics of the NLR as they relate to observations, we construct and analyze velocity profiles for each NLR. From the simulations we have the 3-D velocities for each NL-emitting SPH particle, measured with respect to the stellar center of mass. After projecting these along a given sight line, we assume that within each particle, the NL clouds have an internal velocity dispersion of $0.2 c_{\mathrm{sound}}$. The resulting total velocity profile is then convolved with a Gaussian to degrade it to the desired resolution, chosen to correspond to the spectral resolution of SDSS or DEIMOS at typical redshifts for double NL AGN (we use a fiducial value of 65 km s^{-1}).

3   RESULTS

3.1   Evolution of the Narrow-Line Region in a Major Merger

3.1.1   General Properties

The maximum BH separation for which double NLs could result from BH motion is set by the size of the spectral slit or fiber of the instrument taking the observations. The size of the spectral slit on the DEIMOS spectrograph is 0.75", corresponding to 5.36 kpc at $z = 0.7$. Thus, only a binary BH with separation $a_{\max} \lesssim 5.36$ kpc could be observed to have double NLs with DEIMOS. The diameter of the SDSS spectroscopic fiber is 3", which projects to 5.47 kpc and 21.4 kpc at $z = 0.1$ & 0.7, respectively. Thus, for the mean redshifts of each sample, the double-NL diagnostic is sensitive to binaries with projected separation $\lesssim 5.5$ kpc.

For our analysis of NLRs in galaxy merger simulations, we divide the merger evolution into phases based on these limits for observing double NLs, considering both the maximum BH separation $a_{\max} = 5.5$ kpc, corresponding to systems at $z \sim 0.1$, and a larger value $a_{\max} = 21$ kpc, corresponding to higher-redshift systems. We refer to the early merger stage as Phase I, when the NLRs are well-separated and could not be observed in a single spectrum ($a_{\mathrm{sep}} > a_{\max}$). Phase II we refer to as the "kiloparsec-scale phase", which occurs when the following criteria are met: (i) $a_{\mathrm{sep}} < a_{\max}$, (ii) at least one BH has an active NLR, and (iii) the BHs have not yet merged. We define the post-BH-merger phase as Phase III. If for any period between Phases I & III the Phase II criteria (i) & (ii) are not met, we define this period as Phase IIb.

In Fig. 1, we show the evolution of AGN activity and the NLRs throughout a major merger. The Hβ luminosity traces the bolometric luminosity; both curves have (Eddington-limited) peaks after the first pericentric passage of the two galaxies and a larger peak during the final coalescence. Note, however, that the NLR is not active at all for the first 600 Myr of the merger simulation, owing to the low BH luminosity. Only after the galaxies undergo a close pericentric passage is the BH luminosity high enough for the gas particles to meet our minimum criteria for an active NLR. At the end of the simulation, 200 Myr after the BH merger, L_{bol} and $L_{\mathrm{H}\beta}$ have passed their peaks and begun to decline. Note that the two NLRs have comparable Hβ luminosities, within a factor of ten, throughout most of the simulation (as do the two AGN), though they differ by about to two orders of magnitude for short periods of time. We do not require that the total Hβ luminosities from each NLR be comparable in order to produce dNLs, or even that both NLRs be active. In practice, we find that dNL AGN usually occur when both NLRs are active, though their Hβ luminosities may differ substantially.

Fig. 1 also demonstrates a critical feature of AGN triggered by mergers: peak AGN and NL activity typically occurs during the final coalescence of the two galaxies. Under the assumption of efficient BH mergers, this means that peak activity also roughly coincides with the BH coalescence. This is a well-known result, but it has profound implications for the observability of dual AGN. In essence, merger-triggered AGN are typically brightest both shortly after the BHs have merged and during the kiloparsec-scale phase of BH inspiral. We will see in § 3.4 that this simple fact helps to enhance the probability of observing dNL AGN in the kpc-scale phase versus earlier stages in the merger.

Another notable feature in Fig. 1 is the small gap and dip in $L_{\mathrm{H}\beta}$ that occur near the time of BH merger and peak L_{bol}. This is also when the central gas density in the merger remnant reaches
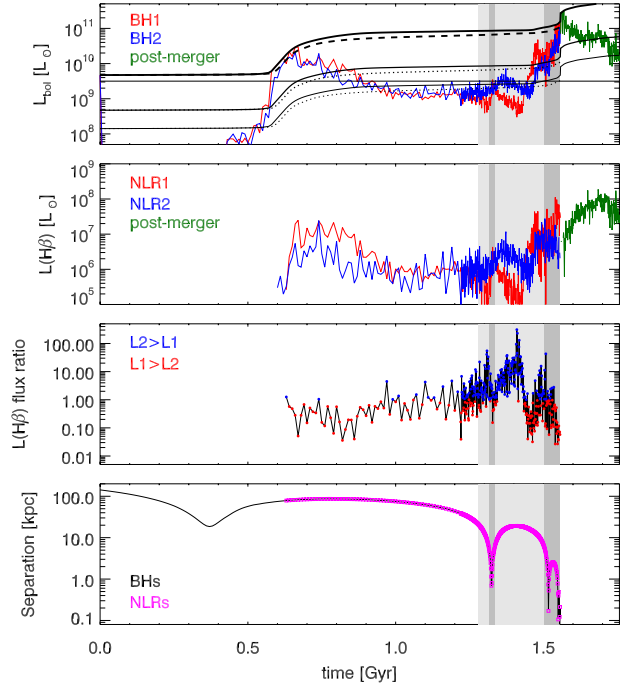

Figure 1. Time evolution of relevant quantities for an equal-mass merger containing 10% gas initially. In each panel, the gray-shaded regions denote Phase II, i.e., the kpc-scale phase. The dark-gray shade denotes BH separations of < 5.5 kpc, which corresponds to the size of the SDSS spectroscopic fiber for objects at z 0.1, or the size of the DEIMOS spectral slit for objects at z 0.7. The light-gray shade denotes BH separations of < 21 kpc, corresponding to the size of the SDSS fiber for objects at z 0.7. Top plot: bolometric luminosity (L_{bol}) versus time. Blue and red curves denote each BH's luminosity prior to the BH merger, and the green curve denotes L_{bol} after the merger. The thick solid and dashed lines (uppermost) denote the Eddington limit for each BH, and the thin solid and dotted lines denote three different definitions of an AGN (3% L_{Edd} and 10% L_{Edd} for each BH, as well as a constant-luminosity definition of 3×10^9 $L_{\odot}$). Upper-middle plot: Hβ luminosity ($L(\mathrm{H}\beta)$). Same color scheme as in top plot. Lower-middle plot: Ratio of $L_{\mathrm{H}\beta}$ for each BH. Points where $L_{\mathrm{H}\beta 2} > L_{\mathrm{H}\beta 1}$ are shown in blue, and those where $L_{\mathrm{H}\beta 1} > L_{\mathrm{H}\beta 2}$ are shown in red. Bottom plot: BH separation vs time. The magenta points denote the NLR center-of-mass separation versus time for the snapshots in which both NLRs are simultaneously active.

its peak, and for a brief time the gas densities surrounding the BHs exceed our maximum density criterion for NLR particles. As described in § **??**, in such conditions the emission from collisional de-excitation begins to outweigh forbidden-line emission, so this gas cannot be considered part of the narrow-line region as it is typically defined for an AGN (with, e.g., [O III]/H$\beta \gtrsim 3$). This gap in NL emission occurs only in the mergers that attain the highest peak densities, i.e., those with nearly equal mass and moderate-to-high gas fractions. Without arbitrarily high-resolution simulations or radiative transfer calculations, it is difficult for us to say exactly what the emission from this region would look like in reality at these moments of peak density. However, it seems plausible that even if a decrement in luminosity does not occur for permitted lines such as Hβ, this could occur for forbidden lines such as [O III] when the gas density exceeds their critical densities. In any case, because these gaps in emission are brief, they do not affect our results qualitatively and could have at most a small effect on our quantitative results (i.e., dNL AGN lifetimes; see § 3.4). [**Note:**
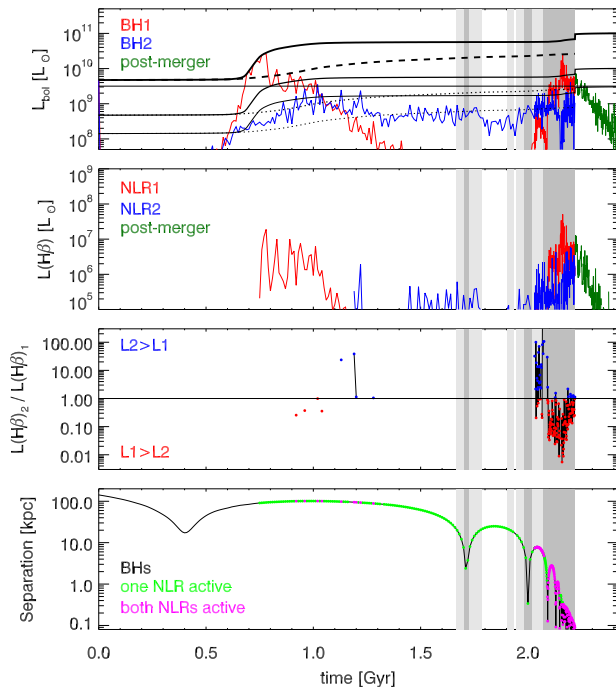
Figure 2. Same quantities as in Fig. 1, but for a merger model with a mass ratio $q = 0.5$ and initial gas fraction $f_{\rm gas} = 0.04$.

My current choice of max. density, 10^6 cm^{-3}, is reasonable because it corresponds to the critical density for [O III] and because it gives more or less reasonable results. However, because the best choice of max. density is a bit unclear, and because in the highest-$f_{\rm gas}$, equal mass run there is a slightly larger gap in Hβ emission that might beunphysical, I am considering increasing the max. density from 10^6 to 10^7 cm^{-3}. I welcome feedback on this matter.

The total merger time from the start of the simulation to the time of BH merger is 1.6 Gyr, but Phase II, shaded in light and dark gray for $a_{\rm max} = 21$ and 5.5 kpc, respectively, has a duration of only **[??]** or **[??]** Myr. In general we find that the BHs, and their NLRs, evolve rapidly to small separations once they enter the kpc-scale phase during the final coalescence of the two galaxies. This is a consequence of efficient dynamical friction and gas drag in the dense merger remnant potential, and it ensures that Phase II is always a small fraction of the total merger timescale.

We use progenitor galaxies that initially have between 4% and 30% of their baryonic mass in gas. This gas is depleted substantially via star formation during the course of the merger; by the time Phase II is reached, the gas content is typically about half of its initial value. However, major mergers are efficient at rapidly fueling gas to the central regions of galaxies, such that the remaining gas in Phase II is concentrated near the center of each merging galaxy. **[Give some data on what fraction of the gas is in the central kpc or so, and what fraction of the mass within that radius is gas vs. stars. The bottom line is that newly-formed stars dominate the central region; will either just say this or show a density profile plot.]**

3.1.2 Dependence on Merging Galaxy Parameters

We find that the amount of NL activity in a galaxy merger is strongly influenced by the galaxy mass ratio and gas content. Fig. 2 shows the same quantities as Fig. 1, but for an unequal-mass merger ($q = 0.5$) with a low initial gas fraction of $f_{\rm gas} = 0.04$. The BH in the primary galaxy has an Eddington-limited burst of accretion following the first close passage, triggering strong feedback that heats the surrounding gas and limits further accretion until final coalescence. The secondary BH never reaches its Eddington limit but maintains a fairly constant $L_{\rm bol}$ following the pericentric passage until final coalescence. While at least one of the NLRs is active for most of the simulation, they are simultaneously active virtually only during the kpc-scale phase, and even then the $L_{\rm H\beta}$ ratio fluctuates widely. Notably, in this example the peak of AGN and NL activity occurs several tens of Myr prior to the BH merger, and thus most of the NL activity coincides with the kpc-scale phase. In contrast, the peak $L_{\rm bol}$ in example in Fig. 1 is nearly simultaneous with the BH merger. Nonetheless, we see that substantially less NL activity occurs in this low-$f_{\rm gas}$, unequal-mass merger than in the previous example. This holds true of our merger models in general; mergers with lower mass ratios and gas fractions have less AGN and NL activity, and thus are less likely to produce observable dNL AGN. (See § 3.4 for a comparison of dNL lifetimes.) This is unsurprising, as equal-mass mergers induce the strongest perturbations in the merging galaxies, causing more gas to lose angular momentum and flow rapidly to the galaxy centers. Galaxies with substantial gas reservoirs will likewise provide more fuel to the central BHs than those that are gas-poor.

An important caveat to this picture of AGN and NL activity in mergers is that these same processes can also trigger rapid star formation, which may produce large amounts of dust that could obscure activity in the central region. The problem is especially complex for the NLR, which is at large enough radii to be intermingled with the newly-forming central cusp of stars. Because the present work, as a first attempt to model the NLR in galaxy mergers, does not account for the potential effects of dust obscuration, we must consider this a substantial caveat to interpretations of our simulated NLRs as "observable". In order to avoid as much as possible a strong-starburst regime, we do not consider initial gas fractions above 30%, and much of the analysis presented here concerns galaxies with $f_{\rm gas} \leq 0.1$. Thus, our simulations produce low- to moderate-luminosity AGN, rather than extreme quasars. Furthermore, while the peak SFR following the first pericentric passage can be in excess of 100 M$_\odot$ yr^{-1} for higher-q and $f_{\rm gas}$ simulations, the peak SFR during final coalescence (i.e., during Phase II) is typically much lower, $\sim 10 - 20$ M$_\odot$ yr^{-1} for these same simulations. For lower-q, $f_{\rm gas}$ mergers, the peak SFR is much lower than this; the example in Fig. 2 has a peak SFR at coalescence of only 0.4 M$_\odot$ yr^{-1}.

As mentioned in § 3.1.1, the peak BH accretion rates generally display the opposite trend; they are higher during final coalescence of the galaxies than following the first close passage. This owes in large part to the fact that the BH masses, which are initially quite small, are typically 1 - 2 orders of magnitude larger at coalescence than at the first passage. Thus, their Eddington limits are larger by the same factor. (The Bondi accretion rates increase with the mass squared, but of course depend heavily on environment as well.) In most of our simulations, the BHs experience Eddington-limited bursts of accretion following the first passage and at coalescence, as in the example in Fig. 1. However, in mergers with lower q and $f_{\rm gas}$ the BHs may not reach the Eddington limit, or they may have a

burst of accretion and feedback early in the merger that heavily depletes the central gas reservoir. In these cases the AGN lightcurve may not have its highest peak during coalescence, as in the example of Fig. 2. In such cases the NL activity is also fairly low, however, indicating that such mergers contribute relatively little to the population of dNL AGN. This therefore supports our argument in § 3.1.1 that most observable dNL AGN triggered by mergers should occur in the late stages of merging, in Phases II and III.

In addition to examining trends in NL activity with galaxy mass ratio and gas content, we also consider the possible relevance of other parameters. First, we consider the addition of a stellar bulge component to our progenitor galaxies, which are nominally pure disks. It is well-known that the presence of a bulge can act to stabilize a galactic disk to perturbations during encounters, thereby delaying catastrophic loss of gas angular momentum until the final coalescence of the galaxies. Much of the star formation and BH growth triggered by gas inflow is thereby similarly delayed. We consider bulges containing 10 - 20% of the total stellar mass, and find that the SFR and BH accretion rate are lower following the first passage and are slightly higher during coalescence. The effect is stronger for the SFR and for higher $f_{\rm gas}$; the peak SFR can change by a factor of several in each direction. However, because AGN and NL activity is generally highest during coalescence in any case, the presence of a bulge only enhances this effect. [**give more quantitative info here.**] Additionally, the higher SFR at coalescence may lead to more obscuration of the NLR during the kpc-scale phase, thereby counteracting to some extent any increase in observable dNL AGN lifetimes.

[**Will also discuss galactic orbits. Early tests at lower resolution indicated that different orbits produce some scatter in the results but are less important than mass ratio and gas fraction. My fiducial orbit is a tilted configuration without any "special" alignment, meant to be fairly generic. I'm currently running a high-resolution simulation with a different orbit, just for completeness, and will add some comment about the results of that run.**]

3.2 NLR Morphology

Here we examine in detail the size, structure, and Hβ luminosity of the NLRs. Fig. 3 shows velocity maps of the NLRs at various stages of the merger, along with corresponding $L_{\rm H\beta}$ maps. The first pair of plots shows a snapshot about 150 Myr after the onset of NL activity following the first close passage of the galaxies. We see that the each NLR is $\gtrsim 500$ pc across, has a disky structure as seen in the xz projection, and is in rotation. Additionally, in the first galaxy (left panels in each plot), a gap in the NLR is seen in the disk midplane. Because the gas density is highest along the midplane, the NL clouds are more easily self-shielded here, and some of them may exceed our maximum-density criterion as described above. The next pair of plots (top right) shows a snapshot later in the merger, when $L_{\rm bol}$, $L_{\rm H\beta}$, and the gas density are near their minima between the first passage and final coalescence of the galaxies. Accordingly, the NLRs are fainter and more diffuse and extended, $\gtrsim 1$ kpc across. Note that the same disk-line structure is still apparent, however. In the following snapshot (middle-left pair of plots), the NLRs are shown during a pericentric passage ~ 200 Myr prior to BH merger; the BH separation here is [**??**] and thus the merger has entered Phase II. Unlike the first two snapshots shown, the BHs show strong relative motion apparent in all three projections, and the corresponding relative motion of the NLRs is especially apparent in the xz projection. The NLRs are still quite diffuse and faint here, with $L_{\rm H\beta} \sim$ few $\times 10^6$ L$_\odot$.

Soon thereafter, as the galaxies near their final coalescence, the rapid inflow of gas drives up the central gas density. As the next snapshot (middle-right pair of plots) shows, the NLRs become denser, brighter, and more compact. Their shape becomes spherical rather than disk-like, as their size is now limited by the self-shielding criterion described in § 2.3.4. Strong rotation features are still apparent, though overall blue- and redshifts are also seen in the xz projection for each galaxy, respectively, owing to their relative motion. The latter feature is greatly magnified in the next snapshot (lower-left plots), occurring just before a close passage of the BHs, 42 Myr prior to their merger. As in the previous close-passage snapshot, strong relative motion is apparent in all three projections, but here $L_{\rm bol}$ and $L_{\rm H\beta}$ are about 10 times higher. This is in fact an example of a double-peaked NL AGN induced by BH motion, as will be discussed in the next section. Finally, the last two plots (lower-right) shows the final snapshot of the simulation, 200 Myr after the BH merger. The gas density, $L_{\rm bol}$ and $L_{\rm H\beta}$ have all declined, causing the NLR to again become more diffuse, but still with higher density and Hβ luminosity than in the early-merger phase.

The prominent, persistent rotation of the NLRs in these snapshots is worthy of closer study. If we define the BH radius of influence as the radius at which the baryonic mass surrounding the BH equals twice its mass ($r_{\rm infl} \equiv r(M_{\rm b} = 2M_{\rm BH})$), then $r_{\rm infl}$ ranges from $\gtrsim 100$ pc early in the merger, when the gas density is low, to only a few pc at late stages when the gas density is much higher. Thus, at all times, $r_{\rm NLR} \gg r_{\rm infl}$, so the gravitational potential of the BH alone is not responsible for keeping the NL clouds bound in coherent rotation. However, following the first close passage of the galaxies, a dense cusp of new stars begins to form in the central region of each galaxy. As was discussed in § 3.1.1, this stellar component is dominant within the central $\sim$ kpc. Fig. 4 demonstrates that the kinematics of the NL gas matches that of the central gas distribution, which itself traces the kinematics of the stellar cusp. Therefore, we see that it is indeed the gravitational potential of the newly-formed stars, as well as their angular momentum, that creates the stable rotation features in the NLRs seen in Fig. 3.

A remaining question is whether the softened gravitational potential used in our simulations has a nonnegligible effect on the kinematic structure of the central region. The gravitational softening length used in our simulations is $r_{\rm soft} = 37$ pc, which is smaller than the size of our NLRs, but because of the softening kernel used, the gravitational forces are not strictly Newtonian until $2.8 r_{\rm soft}$, i.e., 104 pc. When the galaxies are near coalescence and the NLRs are most compact, their size can indeed be comparable to this value. We have drawn these two radii, $r_{\rm soft}$ and $2.8 r_{\rm soft}$, on the panels in Fig. 4. In the first example, the central stellar rotation feature is comparable in size to the extent of the softening kernel. However, we have resimulated part of this merger with a softening length five times smaller, and we show the result for the same snapshot in the second plot. Here, the circle drawn at $2.8 r_{\rm soft}$ is barely larger than the size of the dot used to denote the BH position, yet the kinematic stellar structure has the same spatial extent. In fact, the smaller softening length seems to allow the stellar rotation to persist down to smaller scales around the BH. This is evidence that if anything, the gravitational softening "washes out" rotation features on the smallest scales, and therefore is not artificially inducing or supporting rotation on scales of a few 100 pc. In both cases the motion of the gas traces that of the stars, so we can have similar confidence in the rotation observed in our NLRs. Additionally, we find that the central, rotating cusp of stars does not appear until
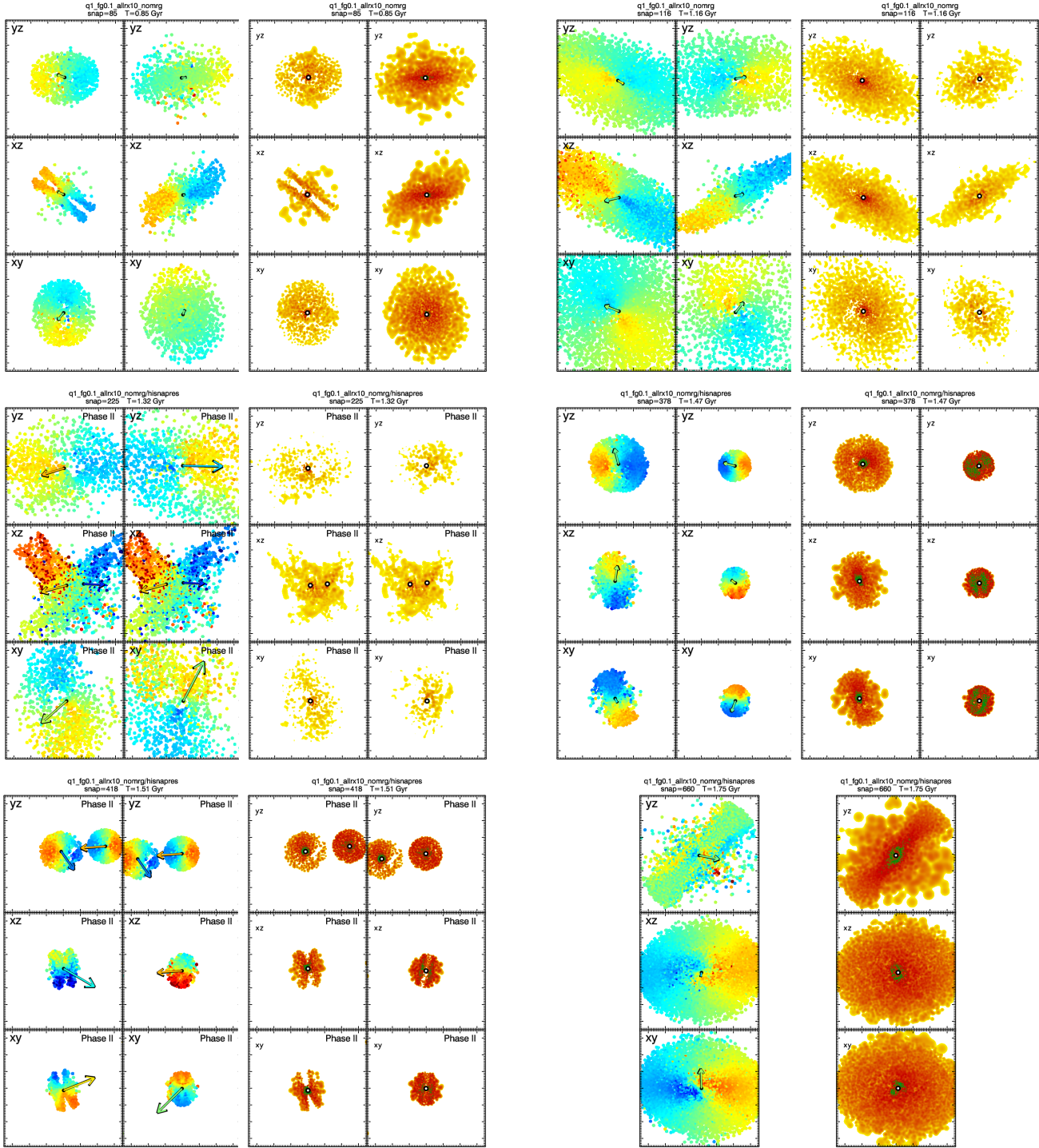
Figure 3. LOS velocity maps and $L_{\mathrm{H}\beta}$ maps of NLRs at six different snapshots throughout a single galaxy merger. In each 6-panel plot, the left column of shows three orthogonal projections centered on BH2, and the right column shows the same three projections centered on BH1. In each pair of plots, the left plot is the velocity map and the right plot is the $L_{\mathrm{H}\beta}$ map. In the velocity maps, the magnitude of the colored arrows denotes the projected BH velocity, and their hue denotes the LOS BH velocity. Each panel is 1 kpc on a side, and the velocity scale spans from -500 km s^{-1} (red) to 500 km s^{-1} (blue). This sign convention for LOS velocity is used throughout the paper. The panels in the $L_{\mathrm{H}\beta}$ maps are also 1kpc on a side. [**Will make color-scale legends for these plots.**]
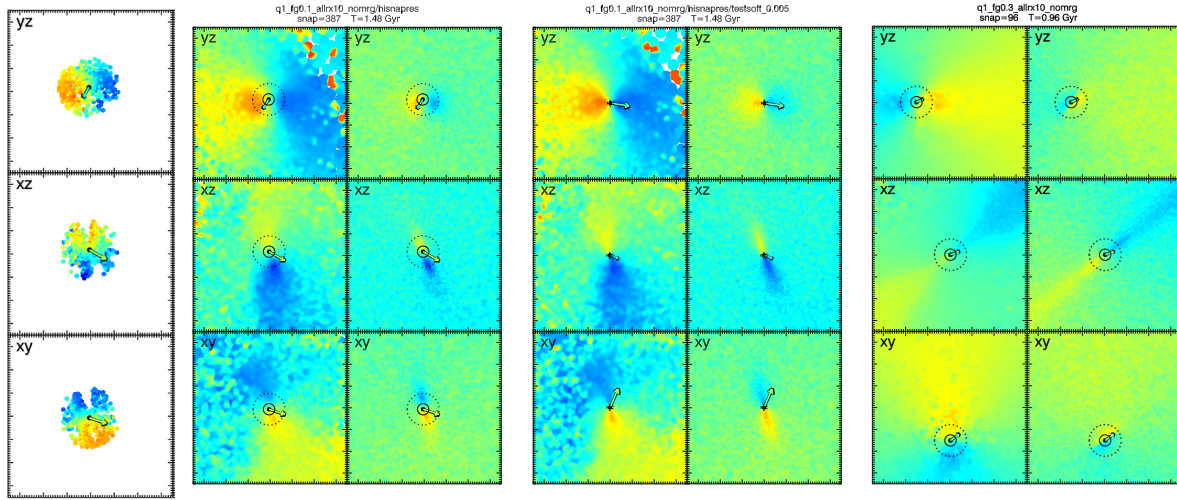
Figure 4. Left plot: Hβ velocity map centered on one BH, in three projections, in a similar manner as in Fig. 3. The BH velocity vectors are also plotted here as in Fig. 3. The simulation shown has $q = 1$ and $f_{\mathrm{gas}} = 0.1$ initially. **Left-middle plot:** For the same simulation, the velocity map is shown for the *total* gas distribution (rather than only the NL gas) in the left panels, and for the total *stellar* distribution in the right panels. The solid circle drawn around the BH denotes the gravitational softening radius (r_{soft}), and the dashed circle denotes $2.8r_{\mathrm{soft}}$, the point at which the gravitational force becomes fully Newtonian. **Right-middle plot**: The same gas and stellar velocity maps are shown as in the previous plot, for the same merger model, but with the merger partially re-simulated with an r_{soft} that is 5 times smaller. The same circles are drawn here, but because r_{soft} is smaller, their size barely exceeds that of the dot that marks the BH position. **Right plot**: The same gas and stellar velocity maps are shown, but for a different merger model with $q = 1$ and $f_{\mathrm{gas}} = 0.3$. The larger gas supply causes enhanced central star formation and a kinematic feature extending well beyond r_{soft}.

after the first burst of star formation following the close passage of the galaxies; prior to this, the velocity map is featureless in this central region. This supports the picture in which a newly-formed cusp of stars supports the rotation seen in the NLRs, and argues against a numerical origin since the gravitational softening remains constant throughout the simulation. Further evidence along these lines comes from the third plot in Fig. 4, which shows a snapshot from an equal-mass merger with a higher gas fraction ($f_{\mathrm{gas}} = 0.3$). In this simulation, the higher gas content provides more fuel to the central regions for star formation, and accordingly a much more extended, disk-like rotating stellar feature can be seen in the velocity map, well beyond $2.8r_{\mathrm{soft}}$. The softening length remains the same in this simulation, so the larger spatial extent of the coherent rotation in this example must result from the larger gas content of the galaxies.

3.3   Observable Signatures of kpc-scale Double-NL AGN

3.3.1   NLR Kinematics

In Figs. 5 - 7, we illustrate some examples of kiloparsec-scale dNL AGN, looking in detail at their kinematic features. Foremost, these examples demonstrate that a variety of velocity structures can give rise to dNL AGN during the kiloparsec-scale phase. All four examples are from the same simulation, with $q = 1$ and $f_{\mathrm{gas}} = 0.1$ initially. Fig. 5 (the yz projection; top panels) is an example of what might be considered the "standard" picture of a dNL AGN. We see two distinct NLRs, one associated with each BH, with NLR LOS velocities corresponding to the substantial LOS velocities of the BHs. The velocity profile (v_x; first column) shows a broad, highly redshifted peak arising from the NLR associated with "galaxy 1", and a similar, blueshifted peak arising from the other NLR. The combined profile, which is what an observer would see, is a wide double-peaked NL with fairly even peaks. This is an example of a

dNL AGN resulting directly from BH motion, at a time when the NLRs are still distinct and non-overlapping.

Fig. 6 also shows a dNL AGN that results directly from BH motion, but in a very different regime. Here, the BH separation is comparable to the size of the NLR, so we would not expect to see two distinct NLRs. In this particular case, the luminosities of the two BHs are substantially different; we see in the middle panels of the velocity profile that the BH associated with galaxy 2 is much fainter. As a consequence, the NLR emission arises almost entirely from ionization by the first BH. However, it is obvious from the velocity map that the second BH is influencing the NLR kinematics as it nearly plows through the NLR. Note that the resulting double-peaked profile is apparent in all three orthogonal projections, owing partly to the rapid relative motion of the two BHs. This is therefore a second example of a dNL resulting directly from BH motion, but at a later stage in the merger evolution when only a single, common NLR remains. It is worth stressing that in this example, a dNL AGN results directly from BH motion even though the BHs do not have comparable luminosities. Indeed, because the second BH is interacting with gas that is ionized by the primary BH, the secondary BH need not even be active to produce this type of kinematic feature. Such features will be very short-lived, of course, but should be hard to avoid once the BH separation falls below the size of the NLR, provided there is sufficient motion in the LOS. This is important for the likelihood of observing such systems, as AGN frequently exhibit variability. Furthermore, in some unequal-mass mergers we find an additional cause of large differences in AGN luminosity between the two BHs. The smaller BH may be partially stripped of its central cusp of gas and stars as it interacts with the larger stellar cusp during the final inspiral phase (on $\sim$ 100 pc scales). This depletes the reservoir of fuel available to the smaller BH, and thus creates a drop in its accretion rate just prior to merger.

In addition to dNL AGN produced directly by BH motion, we find many examples where double-peaked profiles are produced by gas kinematics but are influenced by the BH motion. In other cases,
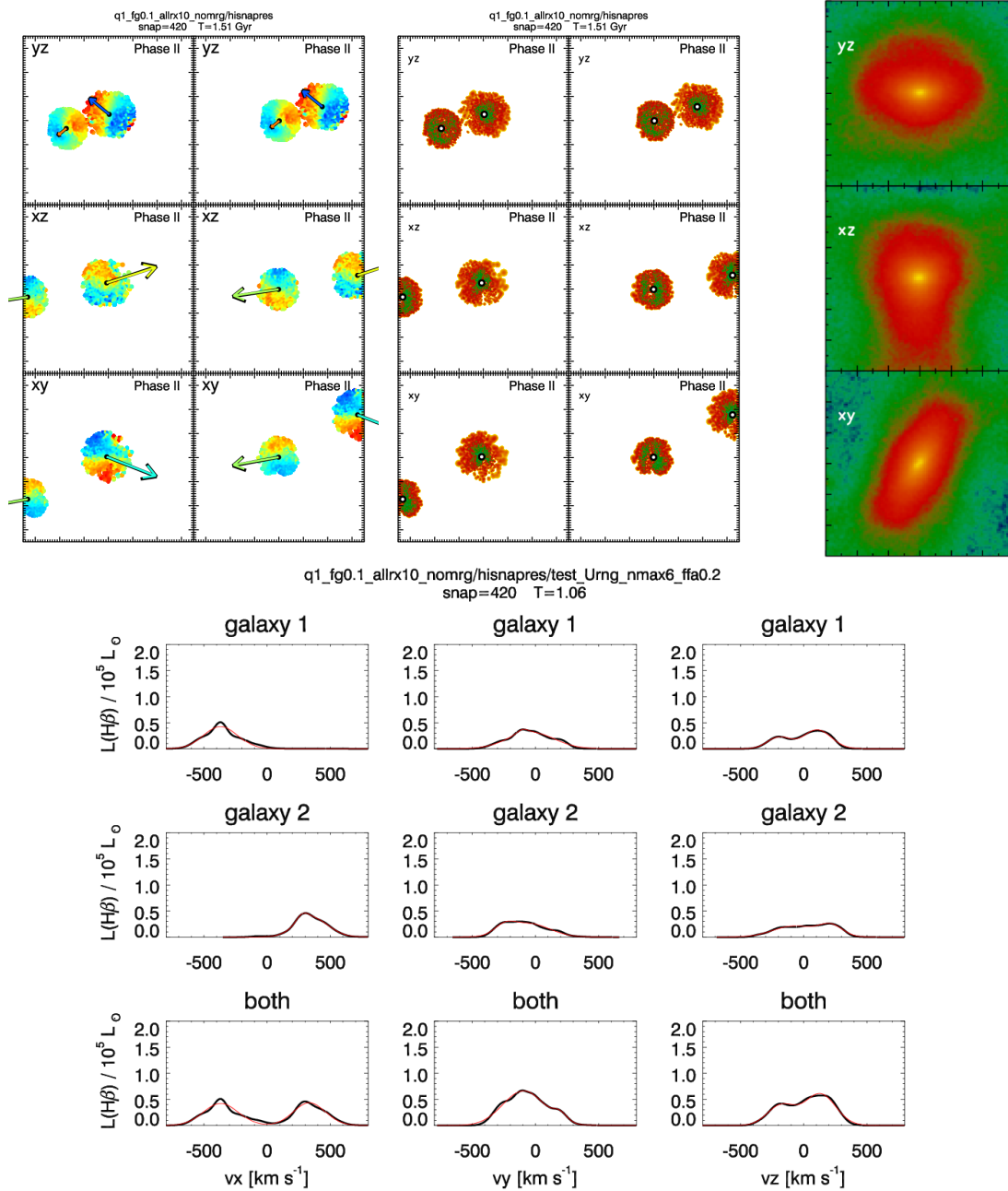
Figure 5. The NLR velocity maps, Hβ luminosity, and 1-D velocity profiles, as well as the stellar density maps, are shown for three orthogonal projections of a single simulation snapshot during the kpc-scale phase (Phase II). The merger model for the simulation shown had $q = 1$ and $f_{gas} = 0.1$ initially. The snapshot shown occurs 40 Myr prior to the BH merger, and the BH separation is [**???**]. **Top left plot**: LOS velocity maps for NLR particles, in the same manner as in Fig. 3. As before, the left column of this plot shows three projections centered on BH2, the right column is centered on BH1, and the arrows denote the BH velocity. **Top middle plot**: map of Hβ surface brightness. The orientation and scale of these panels is the same as in the velocity map (left plot). Here the BH positions are denoted by the black open circle. **Top right plot**: Projected stellar density shown from the same three orientations but on a much larger scale; each panel is 22 kpc on a side. The images are degraded to a resolution of 0.2 kpc/pixel and convolved with a PSF with a FWHM of 0.9 kpc. These values are chosen to correspond roughly to the image quality of a $z \sim 0.1$ source observed with the PANIC near-IR camera on Magellan (with 0.5" seeing), which was used for follow-up imaging of dNL AGN by Shen et al. (2011). **Bottom plot:** 1-D velocity profiles for the NLRs shown. The three columns show v_x, v_y, & v_z, corresponding to the yz, xz, and xy projections, respectively. The top row shows the profiles for NLR particles associated with galaxy 1 (and BH1), and the middle row shows those associated with galaxy 2 (BH2). The bottom row shows the combined profile. Because this snapshot is within Phase II, the combined profile is by definition what would be seen by observers. In each panel, the black line shows the profile calculated from simulation data, and the thin red line is the best fit for a double-Gaussian profile. The calculated profiles assume an internal velocity dispersion of NLR clouds within each SPH particle of 0.2 c_{sound}, and are degraded to a resolution of 65 km s^{-1}.
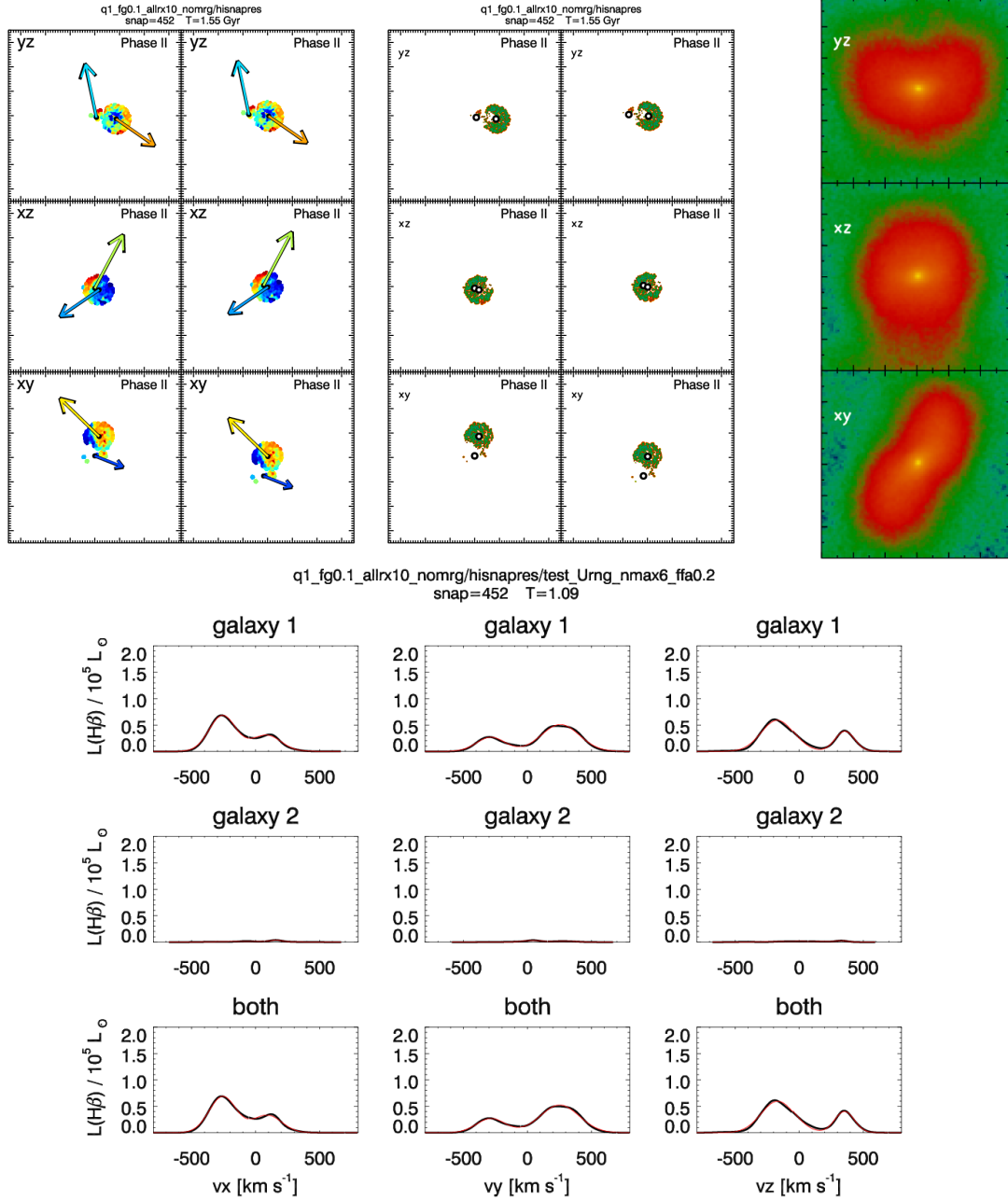
Figure 6. NLR velocity maps, Hβ luminosity maps, and 1-D velocity profiles, as well as stellar density maps, are shown in the same manner as Fig. 5, for a different Phase II snapshot in the same simulation. This snapshot occurs 8 Myr prior to BH merger, when the BH separation is [**???**].

the double-peaked features arising from gas kinematics are simply coincident with the kpc-scale phase; these cases are also of interest, especially as examples of this scenario have already been found in real systems (Fu et al. 2011). Figs. 7 and 8 are examples of the former case, where the BH motion influences a double-peaked profile arising from gas kinematics. In Fig. 7, the xz projection of the velocity maps shows that BH1 has a low velocity and BH2 has a higher velocity. This is reflected in the v_y velocity profile; NLR1 has a double-peaked profile with a peak ratio near unity and little to no velocity offset, while NLR2 has a single-peaked, offset profile. The $L_{H\beta}$ maps and the velocity profiles show that both NLR components have similar peak luminosities. The combined profile is an

uneven-peaked dNL in which the uneven peak ratio is the result of BH motion (in this case, BH2), so although the double-peaked feature arises from gas kinematics, its profile is influenced by relative motion of the BHs.

Another example in which BH motion plays an indirect role in producing dNL AGN is shown in Fig. 8. The xz projection (middle panels) of the velocity plot shows the two NLRs clearly blue- and redshifted, respectively, in accordance with each BH's motion. The $L_{H\beta}$ map shows that the NLR associated with galaxy 1 is significantly brighter than the other NLR. The velocity profiles for v_y show that the brighter NLR has a double-peaked profile arising solely from its internal kinematics, but with an offset (redshifted)
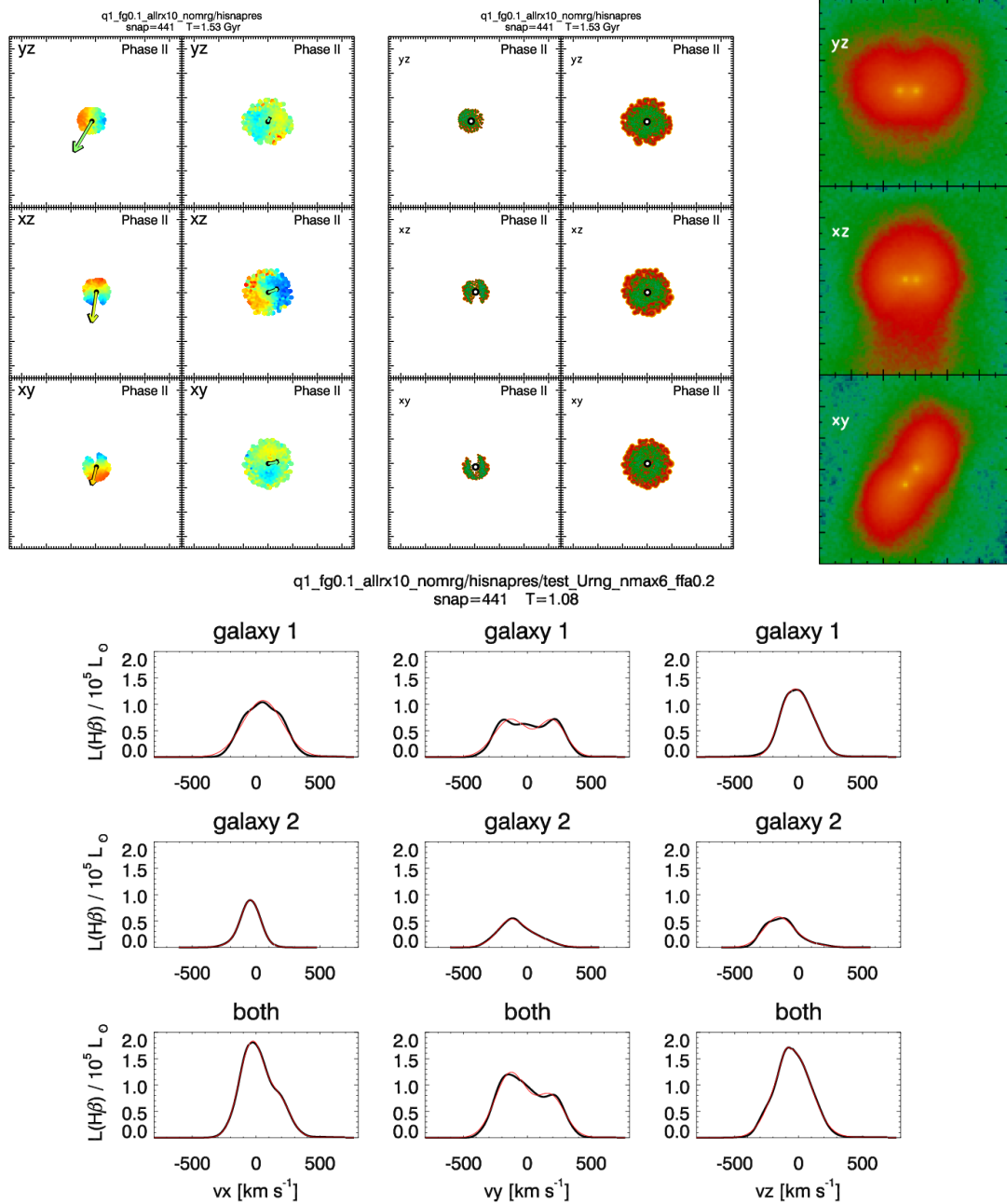
Figure 7. NLR velocity maps, Hβ luminosity maps, and 1-D velocity profiles, as well as stellar density maps, are shown in the same manner as Fig. 5, for a different Phase II snapshot in the same simulation. This snapshot occurs 19 Myr prior to BH merger, when the BH separation is [**???**].

centroid. The fainter NLR (associated with galaxy 2) also has an offset velocity profile, but contributes little to the combined profile. Thus, the combined velocity profile is double-peaked owing to the kinematic structure in an isolated NLR (the brighter of the two), but the overall velocity *offset* of the profile is a direct result of the orbital motion of this NLR (and its BH) in the gravitational potential of the galaxy.

The v_z profile (xy projection) for this same snapshot shows a similar double-peaked profile arising from the NLR associated with galaxy 1, but with no overall offset. The velocity map shows that the LOS motion is much smaller in this projection than in the xz projection. The fainter NLR2 is somewhat offset but again contributes

little to the combined velocity profile. This is therefore an example of a dNL AGN that results from gas kinematics rather than BH motion, but that happens to be coincident with the kpc-scale phase.

We see from these four examples that there are numerous possible origins for kpc-scale dNL AGN. The double-peaked profiles may be a direct result of BH motion, or they may arise from gas kinematics in a single NLR. In the latter case, BH motion may still indirectly contribute to the resulting velocity profile by altering, for example, the line centroid or peak ratio. Finally, some dNL AGN that arise from gas kinematics are simply coincident with the kpc-scale phase, even though the velocity profile contains little to no evidence of the presence of a dual BH. We discuss in the next sec-
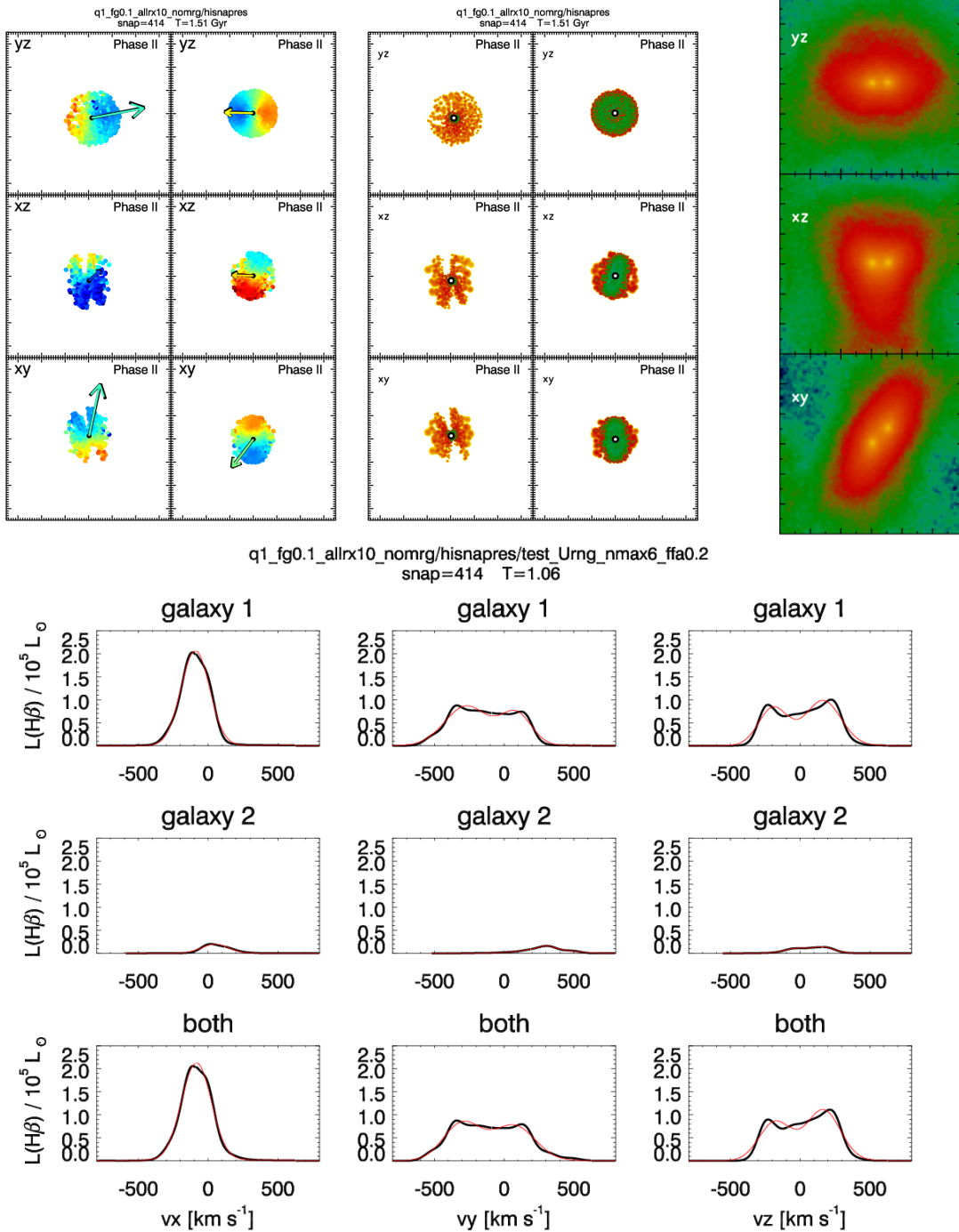
Figure 8. NLR velocity maps, Hβ luminosity maps, and 1-D velocity profiles, as well as stellar density maps, are shown in the same manner as Fig. 5, for a different Phase II snapshot in the same simulation. This snapshot occurs 46 Myr prior to BH merger, when the BH separation is [**???**].

tion the extent to which the observation of such a system is truly a coincidence.

[**Note: As of now I can only discuss qualitatively the distinction between dNL AGN that result directly or indirectly from BH motion, and those that merely coincide with the kpc scale phase. Obviously a robust statistical analysis is impossible, but I plan to try performing a visual analysis of each snapshot in the kpc-scale phase, at least for a couple of simulations,** **to categorize them by hand and estimate the relative likelihood of each type of dNL AGN within a given merger.**]

3.3.2 Stellar Structure

In addition to the NLR kinematics, Figs. 5 - 7 also show the stellar density map for each of these examples. In each case the resolution has been degraded and convolved with a PSF (as described in the figure caption) such that it corresponds roughly to the image quality

of an object at $z \sim 0.1$ observed with the PANIC near IR camera on the Magellan telescope. This is the instrument used by (Shen et al. 2011) for imaging follow-up of dNL AGN. [**Can also discuss other possible instruments for imaging.**] We are able, therefore, to get a sense of whether our dNL AGN would have resolvable dual stellar cusps in such imaging studies, although of course we are plotting surface density as opposed to surface brightness. In Fig. 5, the two stellar cores are marginally resolved in the xy projection, but have a smaller projected separation in the other two projections [**these may also count as marginally resolved, but would need to implement some model fitting to say for sure.**] Specifically, the projection in which the dNL AGN induced by BH motion is apparent (yz) has the smallest of the three projected separations. This is not simply an unlucky coincidence, but rather a fairly common feature of kpc-scale BH pairs. Owing to their rapid inspiral on these scales, their orbits do not circularize. Thus, the largest LOS velocity separation occurs when the LOS is oriented along the long axis of the eccentric, plunging orbit and the BHs are at pericenter, which corresponds to the smallest projected spatial separation. This effect has unfortunate implications for attempts to confirm dual BH candidates via spatially-resolved stellar cusps, but it also leads to the important conclusion that some apparently single-core galaxies may in fact be hiding dual BHs at small projected separation. In such cases, other clues may hint at the object's true nature, however. The yz and especially the xz projections in this example show evidence of disturbed morphology that indicates the galaxy's ongoing merger state.

Fig. 6 is a more extreme example of an unresolved BH pair that nonetheless shows obvious morphological disturbances in its stellar structure. The projected BH separation here is much smaller, $\lesssim 100$ pc, but in two of the three projections the stellar structure is double-lobed on ~ 10 kpc scales (the xz image also shows some disturbance). Galaxies with no apparent double-core structure or disturbed morphology therefore may be more likely to host dNL AGN arising from pure gas kinematics rather than a dual BH. Our findings do suggest, however, that other diagnostics such as high-resolution X-ray imaging may be required to confirm the nature of some dNL AGN. In contrast, the stellar density maps in Figs. 7 & 8 show clearly-resolved double stellar cusps corresponding to the BH pairs at projected separations of several kpc. These are the snapshots in which the BH motion does not directly cause the double-peaked profile but nonetheless influences the profile, by introducing an overall offset or an uneven peak ratio. [**Comment on the fact that the "direct" dNL AGN examples here are unresolvable and the "indirect" ones are. This isn't a true dichotomy in the results as a whole, but the above discussion does indicate that the dNL AGN resulting directly from BH motion may be more frequently unresolvable. This is another reason to do a visual analysis of each snapshot, to attempt to quantify the fraction of dNL AGN of each type that have resolvable stellar cores.**]

3.3.3 Hβ Profile Diagnostics

[**The analysis for this section is still underway; initial attempts to determine trends in the line profile properties based on the LOS-averaged quantities were largely unsuccessful. I am planning to redo the LOS averaging, this time outputting the profile fit parameters for each sight line, rather than just the average and total range. In the meantime, two observations resulted from the current analysis. First, as expected, the Hβ peaks show notably larger offsets during close passages of the two BHs. Second, I see a hint of evidence that the flux ratio of double-peaked profiles is more likely to be uneven during Phase II than at other times, but this is a very tentative statement. I would like to be able to make a stronger statement about the peak ratios, because this has been suggested as a possible diagnostic between dNL AGN that have dual BHs and those that do not.**]

3.4 Lifetimes of Double-NL AGN

Fig. 9 shows the time for which the NLRs have an observable double-peaked profile ($t_{\rm dNL}$) in each merger phase, for eight different galaxy models. In each case, the values shown are averages resulting from fitting profiles for 40 random sight lines in each snapshot, and the division into merger phases is based on the projected BH separation along each sight line. The error bars in each case denote the total range of values for the sight lines sampled. Additionally, as described in § 3.1.1, we consider two different definitions of Phase II; i.e., we use two values of $a_{\rm max}$, the maximum projected BH separation at which both BHs could be observed in the same spectrum. The top and bottom panels of each plot in Fig. 9 give $t_{\rm dNL}$ for $a_{\rm max} = 5.5$ & 21 kpc, respectively. The former definition corresponds to AGN at $z \sim 0.1$, while the latter corresponds to AGN at higher redshifts, up to $z \sim 0.7$. We can see readily that the definition of Phase II does not affect our results qualitatively, with the exception of the highly-variable Phase IIb. More importantly, the amount of variation in merger phase duration and in $t_{\rm dNL}$ for different values of $a_{\rm max}$ is well below the variation for different sight lines.

Each bar on the plots in Fig. 9 shows the total phase duration and is subdivided into the total dNL lifetime (magenta) and the total dNL AGN lifetime (green), according to three different minimum $L_{\rm bol}$ values for defining an AGN. As one might expect, when the Hβ line flux is above the minimum observable criterion, the continuum flux is almost always bright enough to be classified as an AGN. Nonetheless as this is not true 100% of the time, and because the AGN criteria are free parameters in our analysis, we retain the distinction between a double NL with peak $L_{\rm H\beta}$ exceeding a minimum luminosity and a double NL AGN that additionally exceeds a minimum $L_{\rm bol}$.

Comparing $t_{\rm dNL}$ in each phase, we see that in nearly all simulations, Phase III (the post-BH-merger phase) has the longest average $t_{\rm dNL}$. These lifetimes are typically 10s of Myr, but range from zero to nearly 200 Myr (the total duration of Phase III, at which point we stop the simulation) for the merger models and sight lines shown. Phase II has somewhat shorter dNL lifetimes, typically a few Myr to a few 10s of Myr, but ranging from 0 - 65 Myr. Note that in mergers with higher q and $f_{\rm gas}$, the Phase II definition with $a_{\rm max} = 21$ kpc results in longer Phase II dNL lifetimes. For the $q = 1$, $f_{\rm gas} = 0.3$ merger, the increase is a factor of almost three. For mergers with lower q and $f_{\rm gas}$, however, the Phase II definition has little to no effect on $t_{\rm dNL}$ in Phase II. The duration of Phase IIb, however, is strongly dependent on $a_{\rm max}$ and on the line of sight; along some sight lines it doesnt exist at all, and Phase II spans the entire time between Phases I & III. We see also in Fig. 9 that much of the increase of $t_{\rm dNL}$ in Phase II for $a_{\rm max} = 21$ versus 5.5 kpc comes from periods defined as Phase IIb via the latter definition. Again, this variation in the relative duration of Phases II and IIb is substantially smaller than the fundamental uncertainty caused by viewing-angle dependence.

$t_{\rm dNL}$ for Phase I is also somewhat variable, but is usually shorter than $t_{\rm dNL}$ for Phase II. This is contrary to what one might naively assume, because the total duration of Phase I is quite long,
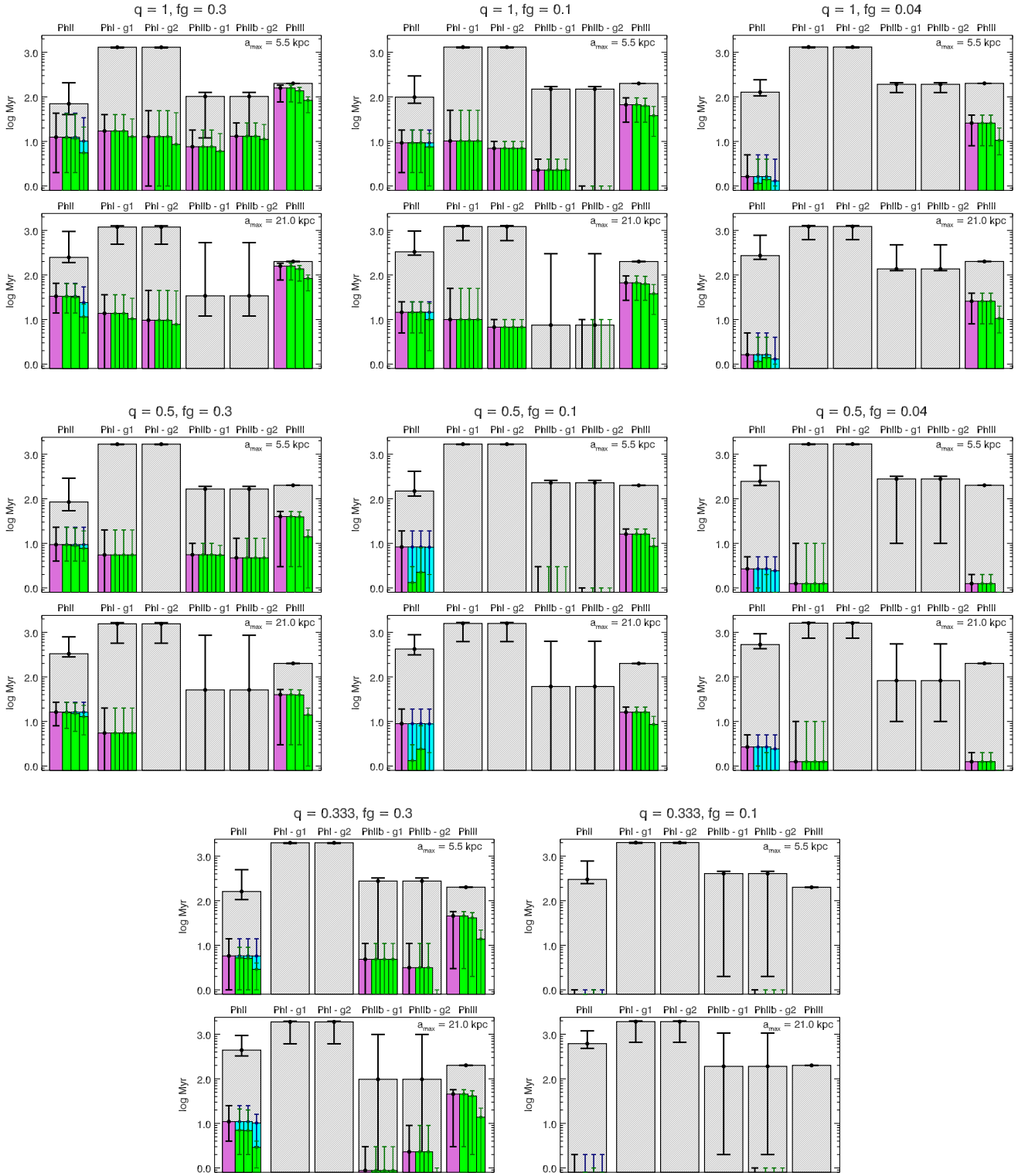
Figure 9. The total time during the merger, separated by merger phase, for which the NLRs have an observable double-peaked profile ($t_{\rm dNL}$). Data are shown for eight simulations with different galaxy models, with q and $f_{\rm gas}$ values as indicated on the plots. Within each panel, Phase II (the kpc-scale phase, as defined in the text) is shown in the first large bar (thin black line), followed by Phase I, Phase IIb, and Phase III. Phase I and Phase IIb are separated into galaxy 1 (g1) and galaxy 2 (g2), as during these phases the NLR from each galaxy would not be observable in the same spectrum. The height of each bar represents the total duration of each phase; note that Phase I is typically > 1 Gyr and thus outside of the plot range. Within each large bar, the smaller bars are as follows. The cyan bar is the mean $t_{\rm dNL}$ within each phase, averaged over 40 random sight lines. The blue error bars denote the entire range of values. Similarly, the green bars denote the mean (line-of-sight averaged) $t_{\rm dNL}$ for which the continuum luminosity exceeds our AGN criteria ($L_{\rm bol} > L_{\rm min}$). The three green bars show the result for three different values of $L_{\rm min}$: from left to right, $10^{9.5} L_\odot$, $0.03 L_{\rm Edd}$, & $0.1 L_{\rm Edd}$. The error bars again denote the range of values for the sight lines sampled.

in excess of 1 Gyr. As discussed in § 3.1, $L_{\rm bol}$ and $L_{\rm H\beta}$ peak first during Phase I (after the first pericentric passage of the galaxies) and again during Phases II & III (during final coalescence). Although $L_{\rm bol}$ is Eddington-limited for a brief time during each peak, the Eddington limit is nearly ten times higher during coalescence, owing to the BH growth in the meantime. Accordingly, the NLRs are also generally less luminous during Phase I and the lifetime of observable double-peaked NLs is shorter, despite the fact that the *total* duration of Phase I is much greater than the combined duration of Phase II and Phase III. The definition of Phase II has little effect on $t_{\rm dNL}$ in Phase I, because the peak of NL activity in Phase I typically happens soon after the first pericentric passage, while the galaxies are still widely separated.

This discussion of the relative duration of double NLs in Phase I versus Phases II & III returns us to a crucial point made in § 3.1.1: the peak of AGN and NL activity generally occurs around the time of the BH merger. Although this is not a new finding, it has important consequences for our present concern, because it means that *double NL activity is likely to be associated with impending or recent BH mergers*. In other words, the time from the kpc-scale phase of BH inspiral through the first few hundred Myr after the BH merger is roughly the time that double NL AGN (and NL AGN in general) are likely to be active. This statement holds *regardless* of whether the double-peaked profiles are a direct result of BH motion or are simply a result of NLR kinematics. The relative lifetimes of Phase II and Phase III depend on exactly when the AGN emission peaks relative to the time of BH merger, and on other factors such as the ratio of Hβ luminosities from each NLR prior to merger. Nonetheless, we see that a "serendipitous" discovery of a dual AGN with a double-peaked profile, but in which the double peak resulted from gas kinematics (cf. Fu et al. 2011), does not seem to be serendipitous after all. Rather, such discoveries are to be expected as a consequence of the timing of the kpc-scale phase relative to the peak of AGN activity.

4 SUMMARY & DISCUSSION

- Summary of main results.
- Discussion of model dependence and validity of assumptions.

  – Resolution dependence and gas equation-of-state dependence

  – Dust obscuration

  – Issues with two-phase ISM model in general (i.e., future work will require more detailed models).

  – Better comparison of my NLRs to observed (beyond e.g., the size and density)

  – Possible sub-resolution kinematics (certainly should occur, but we are most concerned with the phase where the BH motion dominates the kinematics.)

  – BH accretion and feedback - only need a sentence or two.

- The big picture

  – Are dNLs a good tool for finding dual AGN? The situation is messy, with many chances for false positives & negatives, as well as coincidences, but we can say that for merger-triggered activity, dNL AGN are most likely to occur during the late stages of the merger. Those that are not in the kpc-scale phase should be associated with recent BH mergers, which is interesting in its own right.

  – Discuss the possible implications of having substantial post-merger dNL AGN lifetimes. (Relaxed galaxy morphology? GW recoils??)

  – The strength of the previous statement about merger-triggered dNL AGN depends on the frequency of AGN triggered by major mergers vs minor mergers or secular processes. Comment on this and mention recent work (e.g., Ellison et al.) determining the role of mergers.

  – Qualitative discussion of statistics/cosmological context (i.e., frequency of major gaseous mergers, dNL AGN lifetimes, ...)

  – Mention briefly the possibilities for future work, including more detailed ISM models, radiative transfer, and parameter studies.

REFERENCES

Begelman M. C., Blandford R. D., Rees M. J., 1980, Nature, 287, 307
Berczik P., Merritt D., Spurzem R., Bischof H.-P., 2006, ApJ, 642, L21
Bianchi S., Chiaberge M., Piconcelli E., Guainazzi M., Matt G., 2008, MNRAS, 386, 105
Bogdanović T., Eracleous M., Sigurdsson S., 2009, ApJ, 697, 288
Bondi H., Hoyle F., 1944, MNRAS, 104, 273
Boroson T. A., Lauer T. R., 2009, Nature, 458, 53
Comerford J. M., Gerke B. F., Newman J. A., Davis M., Yan R., Cooper M. C., Faber S. M., Koo D. C., Coil A. L., Rosario D. J., Dutton A. A., 2009a, ApJ, 698, 956
Comerford J. M., Griffith R. L., Gerke B. F., Cooper M. C., Newman J. A., Davis M., Stern D., 2009b, ApJ, 702, L82
Dotti M., Montuori C., Decarli R., Volonteri M., Colpi M., Haardt F., 2008, ArXiv e-prints
Escala A., Larson R. B., Coppi P. S., Mardones D., 2004, ApJ, 607, 765
Fu H., Yan L., Myers A. D., Stockton A., Djorgovski S. G., Aldering G., Rich J. A., 2011, ArXiv e-prints
Gerhard O. E., Binney J., 1985, MNRAS, 216, 467
Gould A., Miralda-Escude J., 1997, ApJ, 483, L13+
Green P. J., Myers A. D., Barkhouse W. A., Mulchaey J. S., Bennert V. N., Cox T. J., Aldcroft T. L., 2010, ArXiv e-prints
Komossa S., Burwitz V., Hasinger G., Predehl P., Kaastra J. S., Ikebe Y., 2003, ApJ, 582, L15
Komossa S., Zhou H., Lu H., 2008, ApJ, 678, L81
Liu X., Shen Y., Strauss M. A., Greene J. E., 2009, ArXiv e-prints
Milosavljević M., Merritt D., 2001, ApJ, 563, 34
Rodriguez C., Taylor G. B., Zavala R. T., Peck A. B., Pollack L. K., Romani R. W., 2006, ApJ, 646, 49
Shen Y., Liu X., Greene J. E., Strauss M. A., 2011, ApJ, 735, 48
Shields G. A., Rosario D. J., Smith K. L., Bonning E. W., Salviander S., Kalirai J. S., Strickler R., Ramirez-Ruiz E., Dutton A. A., Treu T., Marshall P. J., 2009, ArXiv e-prints
Sillanpaa A., Haarala S., Valtonen M. J., Sundelius B., Byrd G. G., 1988, ApJ, 325, 628
Smith K. L., Shields G. A., Bonning E. W., McMullen C. C., Salviander S., 2009, ArXiv e-prints
Springel V., 2005, MNRAS, 364, 1105
Springel V., Di Matteo T., Hernquist L., 2005, MNRAS, 361, 776
Springel V., Hernquist L., 2003, MNRAS, 339, 289
Yu Q., 2002, MNRAS, 331, 935